ADVANCED MATERIALS
www.advmat.de

Biomimetic Nanomaterials for the Immunomodulation of the Cardiosplenic Axis Postmyocardial Infarction

Rajendran JC Bose, Chase W. Kessinger, Tajinder Dhammu, Toolika Singh, Miller W. Shealy, Khanh Ha, Rena Collandra, Sebastian Himbert, Fernando J. Garcia, Natalia Oleinik, Bing Xu, Vikas, Maria I. Kontaridis, Maikel C. Rheinstädter, Besim Ogretmen, Donald R. Menick, and Jason R. McCarthy**

Dedicated to essential workers who lost their lives due to COVID-19.

The spleen is an important mediator of both adaptive and innate immunity. As such, attempts to modulate the immune response provided by the spleen may be conducive to improved outcomes for numerous diseases throughout the body. Here, biomimicry is used to rationally design nanomaterials capable of splenic retention and immunomodulation for the treatment of disease in a distant organ, the postinfarct heart. Engineered senescent erythrocyte-derived nanotheranostic (eSENTs) are generated, demonstrating significant uptake by the immune cells of the spleen including T and B cells, as well as monocytes and macrophages. When loaded with suberoylanilide hydroxamic acid (SAHA), the nanoagents exhibit a potent therapeutic effect, reducing infarct size by 14% at 72 h postmyocardial infarction when given as a single intravenous dose 2 h after injury. These results are supportive of the hypothesis that RBC-derived biomimicry may provide new approaches for the targeted modulation of the pathological processes involved in myocardial infarction, thus further experiments to decisively confirm the mechanisms of action are currently underway. This novel concept may have far-reaching applicability for the treatment of a number of both acute and chronic conditions where the immune responses are either stimulated or suppressed by the splenic (auto)immune milieu.

1. Introduction

The spleen is the largest secondary lymphoid organ in the body, which has often been thought of as dispensable, yet its importance as an active regulator of the immune response has only recently come to light.[1–3] Given the tissue's architecture, it increases the likelihood of rare interactions between cells, in particular cognate lymphocytes and antigen-presenting cells.[2] As well, the spleen serves as a reservoir for monocytes capable of trafficking to sites of injury.[4–5] Over the last decade, the importance of the role of this organ in response to ischemic myocardial damage has been investigated.[4,6–9] Upon infarction, increased angiotensin II levels promote the migration of monocytes from the spleen to the heart where they differentiate into macrophages and partake in the inflammatory phase of the insult.[10] Days after the initial injury, the inflammatory milieu changes to one that is reparative, suppressing inflammation and inducing matrix

R. J. Bose, C. W. Kessinger, K. Ha, R. Collandra, B. Xu, Vikas, M. I. Kontaridis, J. R. McCarthy
Department of Biomedical Research and Translational Medicine
Masonic Medical Research Institute
Utica, NY 13501, USA
E-mail: rbose@mmri.edu; jmccarthy@mmri.edu

T. Dhammu, T. Singh, M. W. Shealy, D. R. Menick
Department of Medicine
Division of Cardiology
Medical University of South Carolina
Charleston, SC 29425, USA

S. Himbert, M. C. Rheinstädter
Department of Physics and Astronomy
McMaster University
Hamilton, ON L8S 4M1, Canada

F. J. Garcia
Department of Radiology
Stanford University School of Medicine
Stanford, CA 94305, USA

N. Oleinik, B. Ogretmen
Department of Biochemistry and Molecular Biology
and Hollings Cancer Center
Medical University of South Carolina
Charleston, SC 29425, USA

M. I. Kontaridis
Department of Medicine
Division of Cardiology
Beth Israel Deaconess Medical Center
Harvard Medical School
Boston, MA 02115, USA

M. I. Kontaridis
Department of Biological Chemistry and Molecular Pharmacology
Harvard Medical School
Boston, MA 02115, USA

D. R. Menick
Ralph H. Johnson Veterans Affairs Medical Center
Charleston, SC 29401, USA

The ORCID identification number(s) for the author(s) of this article can be found under https://doi.org/10.1002/adma.202304615

DOI: 10.1002/adma.202304615

deposition and angiogenesis. The spleen's significance in controlling this process is best exemplified by its removal. In inflamed apolipoprotein E-deficient mice receiving a splenectomy before ischemia-reperfusion injury, infarct size was significantly decreased as compared to comparable mice with intact spleens, likely due to a decrease in the initial inflammatory effect.[10]

Histone deacetylases (HDACs) are evolutionarily conserved enzymes that operate by removing acetyl groups from histones and other protein regulatory factors, with functional consequences on chromatin remodeling and gene expression profiles.[11–12] Interestingly, several studies have shown that HDAC inhibition (HDACi) can be beneficial in the setting of myocardial infarction (MI).[12–17] We have previously demonstrated that systemic HDACi via the intraperitoneal injection of suberoylanilide hydroxamic acid (SAHA), a pan-HDAC inhibitor, resulted in decreased inflammatory cytokines and matrix metalloproteinases (MMPs), as well as earlier recruitment of reparative macrophages to the post-MI heart.[12,18] These results correlated well with improved ventricular function and reduced deleterious remodeling. However, the precise molecular mechanism of HDACi and its relation to therapeutic cardiac remodeling is not well understood. Given the established role of the cardiosplenic axis in the provision of pro-inflammatory monocytes, targeted localization of HDACi to this organ may thus be capable of modulating diseases both locally and systemically.[3,6,9] Improving spleen-specific delivery, while decreasing delivery to off-target tissues, has been challenging in the design of nanomaterials.

To accomplish this, we have generated biomimetic nanotheranostics which utilize the spleen's recognition of senescent red blood cells (RBC) to affect enhanced retention of the materials. RBCs, themselves, have been investigated as potential drug delivery vehicles for decades,[19] with more recent examples demonstrating that these cells possess a multitude of capabilities for the localization of therapeutics to sites of action, including as vectors into which drugs are loaded, or via surface modification with proteins or nanoparticles.[20–23] Building upon this earlier work, we have utilized this cell type as a source material for the generation of hybrid nanomaterials. These engineered senescent erythrocyte-like nanotheranostics (eSENTs) utilize flipped RBC membranes featuring unique scavenger signals including the externalization of phosphatidylserine, other oxidized lipids, and senescent cell antigens on their surface, as well as the loss of cell surface CD47, a "don't eat me" signal on healthy RBCs.[24–26] These materials were extensively characterized and their ability to modulate the therapeutic response in a distant organ, in particular scar size and cardiac function after myocardial infarction (MI), was studied.

2. Results

2.1. Generation of Erythrocyte-Derived Materials to Enable Splenic Localization

Heat-damaged erythrocytes (HDE) have been utilized in both preclinical and clinical settings for selective imaging of splenic tissue[27–28] and the splenic retention of HDE can be further modulated by fine-tuning of their physicochemical characteristics such as size, stiffness, and molecular "eat me" signals.[29] Herein, senescent erythrocyte-like ghosts (SEGs) were generated from mouse RBCs by a controlled freezing and thawing (cFT) process (**Figure 1**a).[30] As erythrocytes have a simple structure lacking nuclei and internal organelles, they are highly susceptible to cFT that freezes the cellular water, causing osmotic stress and subsequently leading to cell shrinkage (Figure 1b). Freezing temperatures below −20 °C promote the removal of water molecules associated with the phospholipid head groups, thereby inducing strong fluid-to-gel phase transitions of the erythrocyte lipids, resulting in intracellular ice formation.[31–32] When this is followed by rapid thawing at above 52 °C, hemolysis is accelerated inducing protein denaturation and enzyme inactivation that triggers phospholipid scrambling, thereby promoting the formation of heterogeneous SEGs (Figure 1a,b; and Figure S1, Supporting Information). A subsequent sonication process further reduces the size of SEGs, allowing the spontaneous formation of senescent erythrocytes like nanovesicles (SENVs) which was further confirmed by transmission electron microscopy (TEM) with negative staining and dynamic light scattering (DLS) analysis (Figure 1c,d).

Proteomics characterization of these SENVs revealed that a process combining cFT with sonication (cFTS) induces a significant loss of erythrocyte plasma membrane proteins (Figure S2, Supporting Information) including CD47 (Figure 1e,f; and Figure S3, Supporting Information) and concomitantly concentrates the "eat me" signaling antigenic peptides, including band-3, stomatin, and carbonic anhydrase, on the SENV surface (Figure 1g; and Table S1, Supporting Information). CD47 is a heavily glycosylated cell surface protein present in erythrocytes in a complex with Rh proteins that binds to signal regulatory protein alpha (SIRPα) on immunocytes and suppresses phagocytosis by inhibiting inside-out activation of integrin signaling.[33] CD47 deficient erythrocytes, in particular, are rapidly cleared from the peripheral circulation by splenic macrophages by complement and antibody-mediated mechanisms.[34] Band 3, on the other hand, is the most abundant integral membrane protein in erythrocytes and a member of the anion exchanger gene family (AE-1).[24] Band 3 associates with several other membrane proteins (including CD47, ankyrin, and carbonic anhydrase), with these complexes proving vital in the maintaining of the essential functions of these cells. Yet, its oxidative damage and clustering play an integral role in the signaling responsible for the removal of senescent erythrocytes from circulation.[35–36] Mechanistically, oxidized Band 3 has also been associated with activated complement as an additional mechanism for phagocyte recognition and removal from circulation.[35,37] In fact, in previous work utilizing RBCs as drug delivery vehicles, the authors specifically investigated techniques to prevent complement activation as a result of cell surface modification of with ligands of interest.[38–41] While not investigated further here, complement activation may also play an important role in the observed enhanced splenic retention.

The analysis of lipidomics profiles was subsequently undertaken using a procedure described by Lorent et al. to investigate plasma membrane asymmetry.[42] SENVs were treated with phospholipase A2 or sphingomyelinase to specifically digest only the lipid species present on the exoplasmic leaflet of the vesicle and then analyzed by electrospray ionization mass spectrometry. When compared to the proteins found on the untreated vesicles, the difference in the samples could be attributed to the external lipids. The obtained results reveal that the cFTS

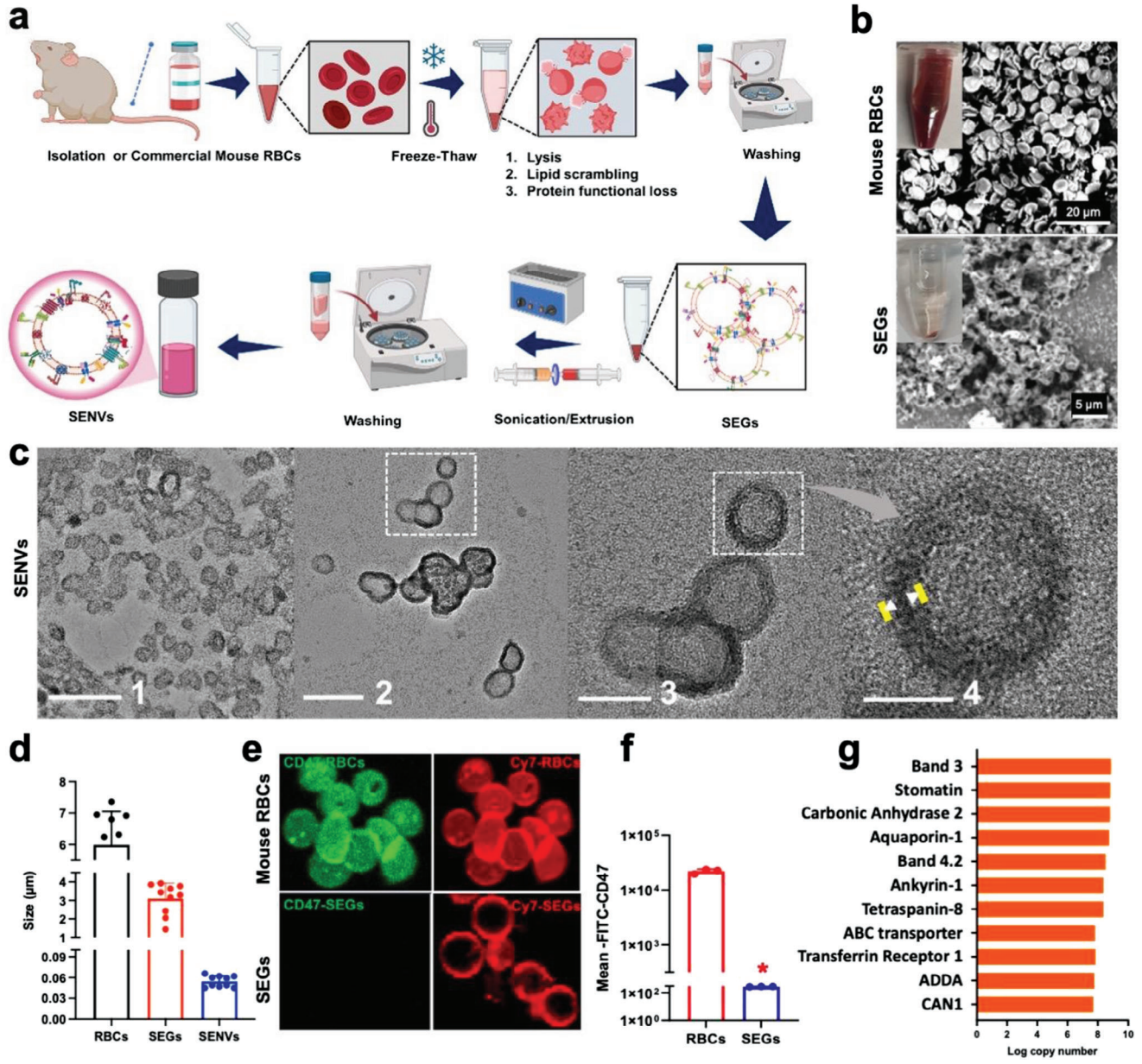

Figure 1. Preparation and characterization of senescent erythrocyte-like nanovesicles (SENVs). a) Schematic diagram outlines the step-by-step preparation process of senescent erythrocyte-like nanovesicles (SENVs). b) Scanning electron micrograph shows healthy RBCs as compared to senescent-like erythrocyte ghosts (SEGs), with the inset showing photographic images of the fresh RBCs and processed SEGs produced by the controlled freeze-thaw with sonication (cFTS) process. c) Transmission electron micrograph shows the SENVs (Scale bar $^{1}200$, $^{2}100$, $^{3}50$, $^{4}25$ nm, respectively) with white arrows highlighting the multilayered nanovesicles. d) Size comparison of mouse RBCs, SEGs, and SENVs. e) Confocal microscopy demonstrates the presence of "don't eat me" signaling protein CD47 on the mouse RBC surface (CD47-FITC – green) and its loss of function on the SEGs surface. Cell membranes labeled with CyAm7 (red). f) Flow cytometry analysis further confirms the presence of CD47 on the mouse RBCs surface, which is diminished on the SEGs. g) LC-MS-based proteomic analysis of SENVs demonstrates how the cFT process concentrates the "eat me" signaling antigenic peptides on the SENVs surface.

process interferes with the erythrocyte plasma membrane asymmetry, scrambling the membranes (**Figure 2**a–c), and modulating the compositional diversity and acyl chain length of the lipids (Figure S4, Supporting Information), which is seen over various scales in sphingomyelins (SMs), phosphatidylcholines (PCs), phosphatidylserines (PS), and phosphatidylinositol's (PIs).[42–43] PS is one of the best characterized membrane-anchored "eat me" signaling lipid molecules, which normally resides on the inner leaflet of the plasma membrane, yet reorganizes to the outer leaflet on senescent and damaged erythrocytes, with this externalized PS binding to receptors on splenocytes to facilitate rapid uptake (Figure S5, Supporting Information).[44] This cFTS process also enhances the formation of immunomodulatory lipids (Figure 2b–d) including lysophosphatidylcholine (LPC), in both

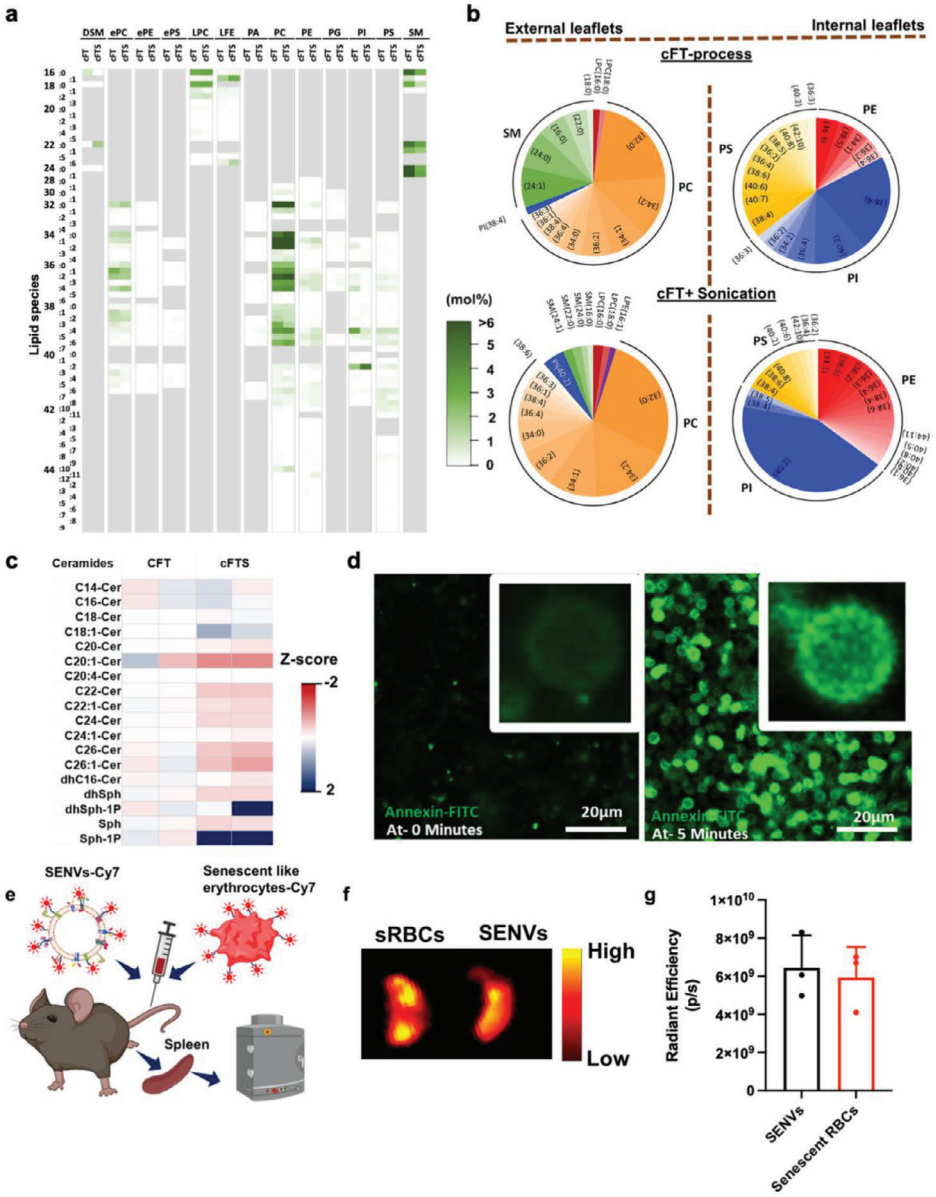

Figure 2. Effect of controlled freeze-thaw process on the erythrocyte membrane lipidomics. a) Lipidomics analysis heatmap demonstrates how the cFTS modulates the process-induced compositional diversity of lipid species. See Extended Data Table S2 (Supporting Information) for an explanation of the abbreviations. Shown in a white-green scale are all lipid species comprising > 0.1-mole percent (mol%) of lipids, with mole percentage encoded in green intensity (darkest = most abundant). Gray indicates species below the 0.1 mol% thresholds (including those not detected). b) Pie chart shows the compiled compositions of the lipidomics analysis of the cFT and cFTS process. c) Lipidomic heatmap shows the process-induced compositional diversity of ceramide lipid species. Shown in a red-blue scale are ceramide lipids species based on Z -Score encoded in red intensity (darkest = most abundant). Dark blue indicates species below the 0.1 mol% thresholds (including those not detected). d) Confocal microscopy-based live sequential images were acquired at 0 and 5 min demonstrating PS lipid externalization via the binding of FITC-labeled annexin-V. E) The schematic diagram outlines the fluorescent labeling of SENVs and senescent-like RBCs (sRBCs). f) IVIS image shows the splenic accumulation of SENVs and sRBCs. g) Quantitative fluorescence image analysis shows the splenic accumulation of SENVs and sRBCs ($n = 3$).

the outer and inner membrane-associated lipid species.[45–46] Additional ceramide-specific lipidomics of the SENVs revealed that cFTS potentiates a membrane rearrangement process, inducing long-chain ceramide derivatives (Figure 2c), which further enhanced the phosphatidylserine migration from the lower to the upper leaflets (Figure 2d; and Figure S6, and Movie S1, Supporting Information).[47,48]

To correlate the materials properties with biological activity, the cFTS-derived SENVs were fluorescently labeled with CyAm7 and injected into naïve C57BL/6J mice, with CyAm7-labeled senescent-like RBCs serving as a control (Figure 2e–g). Forty-eight hours after injection, the animals were sacrificed and the organs were examined for splenic retention, with the SENVs displaying similar accumulation to the source senescent-like

erythrocytes. While it is known that the spleen demonstrates a size-based clearance threshold, for the RBC-derived vesicles used in this study it appears that the surface characteristics of these particles are significantly more critical to splenic immunocyte recognition than their size. Collectively, this data demonstrate that the proteolipids of SENVs afford both the "find me" and "eat me" signals promoting enhanced retention within the spleen (Figure S1b, Supporting Information).

Given these results, we hypothesized that engineering of SENVs to increase the display of PS on the outer leaflet would further enhance splenic accumulation.[49–50] To accomplish this, solutions of SEGs were combined with PS (1,2-dioleoyl-*sn*-glycero-3-phospho-*L*-serine) at three different ratios of SEG lipid to PS lipid via an extrusion and sonication procedure to produced PS lipid engineered SENVs (eSENVs): PS4-eSENVs (4% PS by mass), PS9-eSENVs (9.4% PS by mass), PS16-eSENVs (15.9% PS by mass) (**Figure 3**a).[51] Cryo-TEM analysis revealed the initial formation of heterogeneous PS-modified engineered SEGs (eSEGs, Figure 3b), which were subsequently used to form unilamellar-spherical eSENVs (Figure 3c,d).[52]

2.2. Molecular Modeling of Lipid Bilayer Dynamics

To examine the effect of PS fusion with SENVs, we performed coarse-grained molecular dynamics (MD) simulations (1.5 μs) of the PS and SENVs fusion process, using the results of our lipidomics analysis to modify the input data for the RBC membrane bilayer as a starting point.[53] While electron microscopic images provide details about the vesicle structure and morphology, they are insufficient in understanding the lipid distribution within the synthesized membrane. MD simulations may bridge this gap, as has been shown recently.[54–56] MD models were designed as described in the Supporting Information Experimental Section. 3D renders of the simulated systems are displayed in Figure 3e; and Figure S7 (Supporting Information). Lipids originating in the RBC membrane are visualized as red bonds. PS is visualized in blue bonds. Additionally, the phosphate group of all phospholipids are highlighted as spheres in the respective color. Cholesterol is shown as yellow beads. Although the renderings of the simulation indicate a uniform mixture of erythrocyte membranes with PS, the time averaged density maps show evidence for dynamic nanometer sized patches of PS-rich and depleted regions Figure 3e; and Figure S8 (Supporting Information). The patch sizes were determined as described in the Supporting Information Experimental Section with values of 4.2±1.3/4.0 ± 1.4 nm for the PS16-eSENVs, 2.0 ± 0.7/2.2 ± 0.8 nm for the PS9-eSENVs, 1.1±0.6/1.2±0.3 nm for the PS4-eSENVs (lower leaflet/upper leaflet, Figure S9a, Supporting Information). In addition, the time-averaged largest cluster size of PS was determined using the LiPyphilic library and are graphed in Figure S9b (Supporting Information) as 25±6 lipids/cluster (PS16-eSENVs), 8±2 lipids/cluster (PS9-eSENVs) and 4±1 lipids/cluster (PS4-eSENVs). An overview of the clustering of all remaining lipid species is presented in Figure S9c–e (Supporting Information) which allows for visualization of the enrichment index. Several lipids preferably form clusters. In particular, polyunsaturated lipids (e.g., di-C20:4-C22:5-phosphatidylcholine (DAPC), di-C20:4-C22:5-phosphoethanolamine (DAPE), di-C20:4-C22:5-phosphatidylserine (DAPS), di-C16:3-C18:3-phosphatidylcholine (DFPC), di-C16:3-C18:3-phosphoethanolamine (DFPE), and di-C16:3-C18:3- phosphatidylserine (DFPS)) show a particularly high enrichment index indicating clustering of highly unsaturated lipids in the RBC membrane. This clustering is reduced at higher concentrations of PS. The in-plane diffusion of PS varies slightly with increasing PS concentration. In plane diffusion constants of $2.9 \times 10^{-7} \pm 1.5 \times 10^{-8}$ (PS16-eSENVs), $2.9 \times 10^{-7} \pm 2.1 \times 10^{-8}$ (PS9-eSENVs), and $2.5 \times 10^{-7} \pm 2.7 \times 10^{-8}$ cm^2 s^{-1} (PS4-eSENVs) were determined. Doping the membrane with the monosaturated PS also moderately increases the area per lipid from 0.5746 ± 0.0002 nm^2 in a membrane with a 24.1:1 ratio of RBC:PS to 0.5801 ± 0.0002 nm^2 in a membrane that contains a 5.3:1 ratio of RBC:PS. Details are presented in Figure S10a (Supporting Information). 2D maps, visualizing the in-plane projections of the local area per lipid averaged over the last 100 ns of the simulation are shown in Figure S10b–d (Supporting Information). The area per lipid was found to fluctuate between 0.45 and 0.85 nm^2 which demonstrates a drastic variation depending on the local environment. However, no noticeable difference was observed between the three simulation systems. Previous MD simulations and X-ray diffraction studies on large-scale models show a similar de-mixing of lipid species in biological cell membranes,[57–58] with recent work studying erythrocyte hybrid membranes.[53] The observed lipid rafts are intrinsic to biological membranes and play an essential role in their biological function. The reproduction of rafts in the MD simulations validates the accuracy of these simulations and the model used for RBCs. The formation of PS-enriched rafts indicates the successful incorporation of synthetic PS lipids into the native biological membrane, preserving their structural integrity and dynamics. This is likely crucial for maintaining their biological function and serves as compelling evidence that RBC membranes can be enriched with synthetic lipids. We suggest that the presence of PS-enriched lipid rafts enhances the accessibility and availability of PS for recognition by macrophage receptors, promoting the binding and uptake of red blood cells by splenic macrophages. This mechanism may contribute to the splenic accumulation of red SENVs.

2.3. Splenic Retention of eSENTs

Each of the eSENVs was subsequently utilized to generate the core–shell structure of engineered senescent erythrocyte-like nanotheranostics (eSENTs) by the ES process (Figure 3a,f; and Figure S11, Supporting Information). The cores, which we refer to as NTs, were comprised of poly(lactic-*co*-glycolic acid) (PLGA) nanoparticles, fluorescently labeled with a near-infrared cyanine dye, and were coated with the eSENVs using previously reported strategies,[59–60] increasing the overall hydrodynamic diameter from 104 nm for the uncoated core to 116 nm for the eSENT (Figure S11, Supporting Information). TEM images demonstrated the formation of core-shell hybrid eSENTs featuring an 8–12 nm thick eSENV layer on the surface of the polymeric core (Figure 3f). The process was also accomplished using micrometer-sized PLGA nanoparticles to enable fluorescence microscopic visualization of the resulting materials, including the colocalization of the CyAm7-labeled proteolipids with

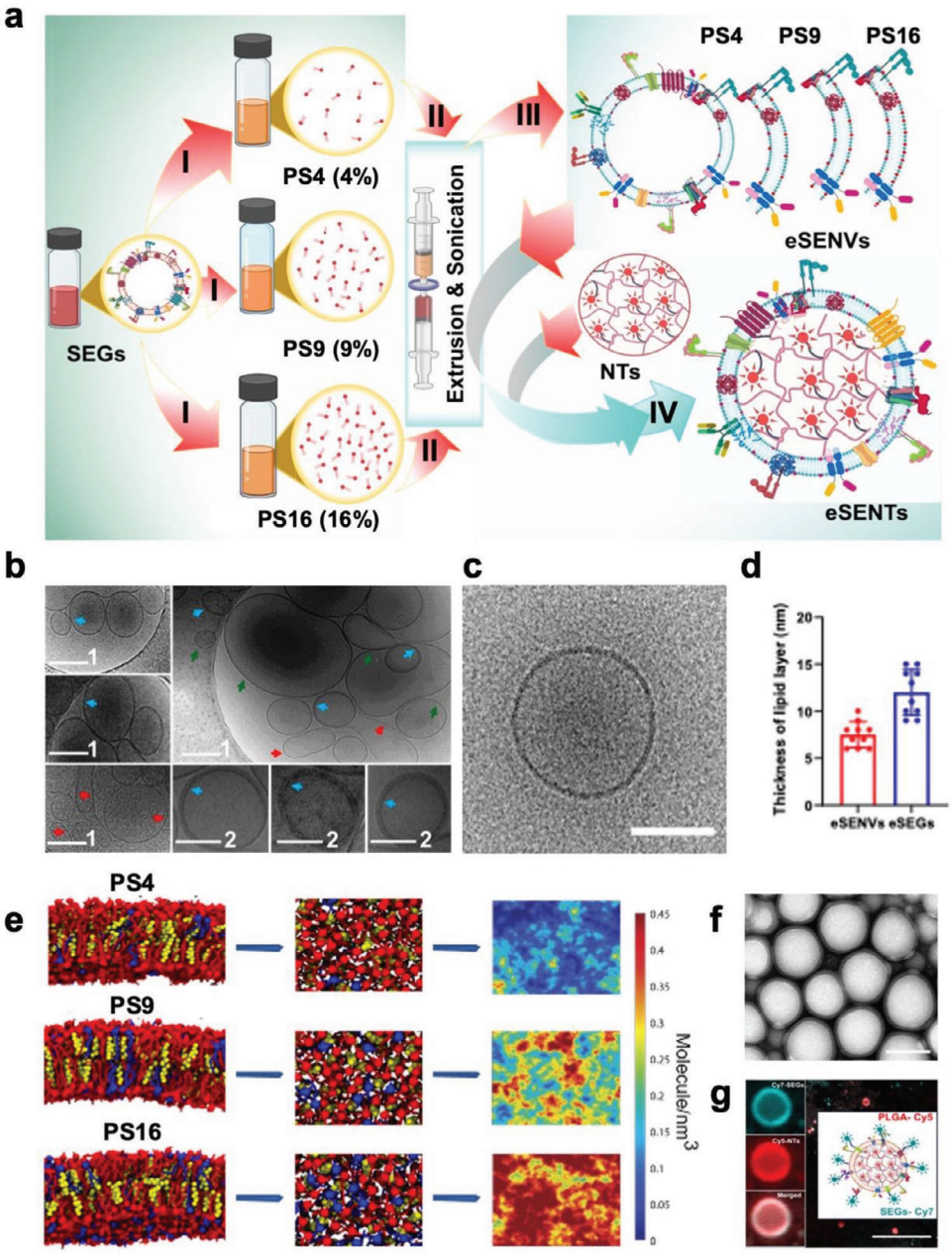

Figure 3. Preparation and characterization of phosphatidylserine lipid-engineered senescent erythrocyte-like nanovesicles coated nanotheranostics (eSENTs). a) Schematic outlines the overall approach used in the design and production of eSEGs and eSENTs. SEGs and PS are combined (I) and processed via extrusion and sonication (II) to give eSENVs (III). eSENVs are subsequently combined with the polymeric core (NTs) via extrusion and sonication to give eSENT (IV). b) Cryogenic TEM micrograph shows the formation of heterogeneous eSEGs (Scale bar [1]100, [2]50 nm, Color code of arrow was used to emphasize the diverse natures of eSEGs: green color represents the heterogenous size of eSEGs; red color represents different shapes of eSEGs; blue color highlights the different degree of lipid layer thicknesses (Insets show the uni- and multilamellar nature of lipids vesicles. c) Sonication, and step-by-step extrusion process yield the unilamellar, spherical nanovesicles of eSEGs (Scale bar 50 nm). d) The thickness of the lipid layer was assayed by cryo-TEM and was analyzed using Image J software (n = 10). e) Course-grained molecular dynamics (MD) simulations (1.5 μs) process were undertaken using the results of our lipidomics analysis to modify the input data for the RBC membrane bilayer as a starting point. Density maps were created to visualize the patchy structure of PS-rich areas in the upper leaflets (shown) and lower leaflets (shown in Figure S8, Supporting Information). f) Negatively stained transmission electron microscopy images of core–shell hybrid nanostructure of eSENTs (Scale bar 100 nm). g) Confocal laser scanning fluorescence microscopy images show the core–shell hybrid nature of the materials produced by the sonication and extrusion process. The micrometer-sized CyAl5-labeled polymeric particles and CyAm7-labeled eSEGs were generated and then fused (Scale bar 20 μm). Inset images show a representative schematic illustration of the core-shell hybrid structure of eSENTs.

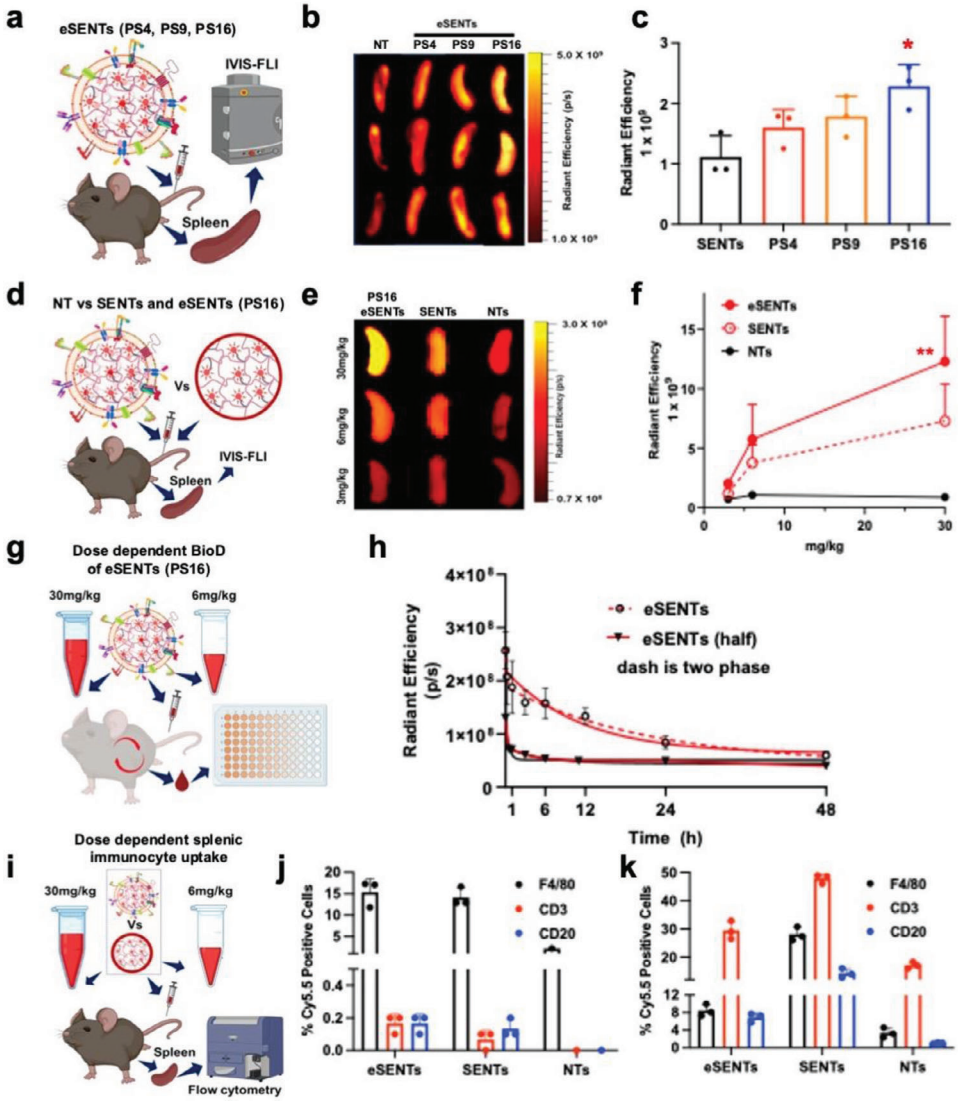

Figure 4. Investigation of the splenic retention of eSENTs in naïve C57BL/6J mice. a) Schematic outline of the PS-dependent splenic accumulation of eSENTs. b) IVIS images show that increases in PS doping result in increased splenic retention. c) Quantitative fluorescence image analysis shows the PS-dependent splenic accumulation of eSENTs (*t*-test,*$p < 0.05$). d) Schematic representation of the comparative experiments between engineered (eSENTs), nonengineered (SENTs), and uncoated nanotheranostics (NTs). e) IVIS images show the comparative accumulation of eSENTs, SENTs, and uncoated nanotheranostics within the spleen. f) Quantitative image analysis demonstrates the superior splenic accumulation of eSENTs versus SENTs, and uncoated nanotheranostics 48 h postinjection as a function of dose (3, 6, and 30 mg kg^{-1}, $n = 3$ mice per group, *t*-test,**$p < 0.05$). g) Schematic outline of the determination of the dose-dependent plasma clearance half-life of eSENTs. h) Quantitative fluorescence analysis illustrates the dose-dependent circulation half-life of eSENTs ($n = 3$ mice per group). i) Schematic representation of the dose-dependent splenic immunocyte-specific uptake of eSENTs. j,k) Flow cytometric analysis of nanoagent (6 and 30 mg kg^{-1}) uptake by splenocytes ($n = 3$ mice per group) depicting the percent of nanoparticle positive cells in the F4/80, CD3, and CD20 gates.

the CyAl5.5-labeled particles (Figure 3g). Preliminary cell uptake experiments with the eSENVs were also undertaken using RAW 264.7 murine macrophages, with the PS-doped materials demonstrating significant uptake by these model immune cells (Figure S5, Supporting Information).

The splenic retention of the resultant eSENTs with differing PS to RBC lipid ratios was initially investigated in naïve C57BL/6J mice, with increases in splenic fluorescence signal correlating with an increased degree of PS doping (**Figure 4**a–c). We next explored whether our observed splenic retention could be modulated by decreasing the dose of the material given, using the highest doped eSENTs versus the undoped or uncoated particles (Figure 4d–f). At the lowest dose (3 mg kg^{-1} polymer) there was no significant difference between groups, whereas a doubling of the dose resulted in dramatically increased signal from the spleen in both coated groups (Figure 4e,f). Moreover, at the highest dose (30 mg kg^{-1}) the eSENTs showed a significantly higher splenic retention (Figure 4e,f) over the control groups. Given the proposed mechanism of splenic accumulation, we hypothesized that the plasma elimination half-life would be relatively short, yet at this

high dose, that was not observed ($t_{1/2}$ = 7.8 h). Based upon prior work in the liver,[61,62] we assumed that we were observing a saturation effect, whereby the organs responsible for the clearance of the nanomaterials were overwhelmed. To test this, we injected the particles at half dose (15 mg kg^{-1}) and observed rapid plasma clearance ($t_{1/2}$ = 0.33 h, Figure 4g,h), intimating that for materials such as these, there may be an active, yet dynamic process responsible for organ retention.

Assessment of the splenic accumulation on the cellular level was accomplished at 48 h after injection using flow cytometric (Figure 4i–k; and Figures S12 and S13, Supporting Information) and histological examinations (Figures S14 and S15, Supporting Information). Injection of these materials, which mimic senescent red blood cells, led to a modulation of the cell types within the splenic milieu, with the most significant changes at the higher dose. In particular, the percent F4/80 positive cells doubled for the eSENTs in the live cell population versus naïve, untreated mice, while the percent CD3 positive cells decreased 20-fold (Figure S13, Supporting Information). While the mechanisms responsible for this effect are still being investigated, we hypothesize that this is a result of the spleen sensing a massive influx of damaged RBCs and responding by increasing the efferocytic capacity as a protective mechanisms with concomitant activation and release of T cells via antigen-presenting cell-based activation. Interestingly, at the 6 mg kg^{-1} dose of particles, eSENTs were mainly localized to F4/80$^+$ macrophages (Figure 4J), yet a fivefold increase in the injected dose (30 mg kg^{-1}), resulted in the material uptake switching mainly to CD3$^+$ T cells and CD20$^+$ B cells (Figure 4k). Immunofluorescence and H&E images further elucidated the intra-splenic accumulation of the particles as being mainly distributed throughout the marginal zone, yet with a minor amount escaping the meshes of the red pulp cords and distributing into the white pulp compartments (Figures S14 and S15, Supporting Information). Overall, these results demonstrate how the rationally designed eSENTs mimic the molecular proteolipid signals of dysfunctional and senescent erythrocytes. Utilizing cell-derived coating materials featuring a functional loss of CD47 and the enriched presence of PS along with oxidized ceramide lipids on the nanomaterial surface leads to enhanced retention and uptake of eSENTs by the various splenic immunocytes in the splenic subcellular compartments.

2.4. Cardiosplenic Axis-Mediated Immunomodulation for the Treatment of Myocardial Infarction

To examine the potential immunomodulatory effect of spleen-localized nanomaterials, we utilized a murine model of myocardial infarction (MI) as shown in **Figure 5**a. As has been demonstrated previously, the spleen serves as a reservoir for monocytes which migrate to damaged tissues in response to injury.[5,63] Inflammatory Ly6C^{high} monocyte recruitment to the infarct area post-MI begins within the first 30 min of ischemic onset and peaks between 48 and 72 h. These monocytes are predominantly recruited from the splenic reserve in a CCR2-dependent manner and differentiate into inflammatory macrophages upon reaching the injured tissue. These early inflammatory macrophages produce high levels of TNF-α, IL-1β, IL-6, MMPs, and reactive oxygen species. The number of Ly6C^{low} monocytes recruited to the post-MI infarct area is initially negligible, slowly increases throughout the first week, and peaks at day 7. This recruitment changes the expression of cytokines, growth factors, pathogen-associated molecular patterns, and other microenvironment mediators shifting macrophage polarization to a less inflammatory and more reparative phenotype.[12,64] In our previous work, we demonstrated that systemic histone deacetylase (HDAC) inhibition via the intraperitoneal injection of suberoylanilide hydroxamic acid (SAHA), a pan-HDAC inhibitor, resulted in decreased inflammatory cytokines and MMPs, as well as earlier recruitment of reparative macrophages to the post-MI heart.[12,18] Importantly, this correlated with improved ventricular function and remodeling. We, therefore, hypothesized that this observed effect was driven by the spleen. Thus, localization of SAHA to this organ may serve to recapitulate the results from the systemic intervention.

To test this, we generated eSENTs containing SAHA within the polymeric core (eSENTs-SAHA) and examined their therapeutic efficacy, with nondrug-loaded particles (eSENTS) and saline injections servings as controls (Figure 5a). Intravenous injection of the immunomodulatory SAHA-eSENTs 2 h after MI significantly increased the number of CD11b$^+$Ly6C$^+$ monocytes/macrophages retained in the spleen (Figure 5b; and Figure S16, Supporting Information). Consistent with this, the number of CD11b$^+$/F4/80$^+$ macrophages present in the infarct at 24 h post-MI were reduced by 3.5-fold when compared to the saline group (Figure 5c; and Figure S17, Supporting Information). While not significant, this trend continued at 72-h post-MI (Figure 5d; and Figure S18, Supporting Information). The data are recapitulated in the 48 h fluorescence-based biodistribution data, exhibiting localization of the eSENTS to the spleen, heart, and lungs of the mice bearing infarcts, whereas those with sham surgeries demonstrated minimal accumulation within the heart (Figure S19, Supporting Information). The fluorescence signal coming from the lung is telling in both groups, as intubation during the ligation of the coronary artery elicits damage to this organ, to which the particles traffic in response to injury. Ultimately, treatment with eSENTs-SAHA dramatically reduced infarct size by 14% at 72-h post-MI when compared to eSENTs or saline controls (Figure 5e,f). Importantly, this significant reduction in ischemic damage was accomplished via a single injection of the SAHA-loaded eSENTs at a drug dose of 3 mg kg^{-1}, as compared to our previously reported 100 mg kg^{-1} day^{-1} required for a similar effect, where it was given systemically.[12,18] The efficacy of the SAHA loaded spleen targeted eSENTs is highlighted by the fact that treatment with the uncoated core PLGA nanoparticles incorporating SAHA (NTs-SAHA) or SAHA-loaded PLGA-cored particles with only PS as the coating material (PS-SAHA) at the same dose demonstrates no significant reduction in ischemic damage when compared to saline controls (Figure S20, Supporting Information). Systemic delivery of the free drug at the same dose (3 mg kg^{-1}) similarly elicited no therapeutic effect (Figure S20, Supporting Information). Most importantly, daily treatment with eSENT-SAHA significantly preserved ejection fraction at 7 days post MI as compared to empty eSENT control (Figure 5G). Taken together, this study serves as the first of its kind to demonstrate the potential of the spleen-targeted inhibition of HDACs in the attenuation of post-MI ischemic damage and the promotion of infarct healing.

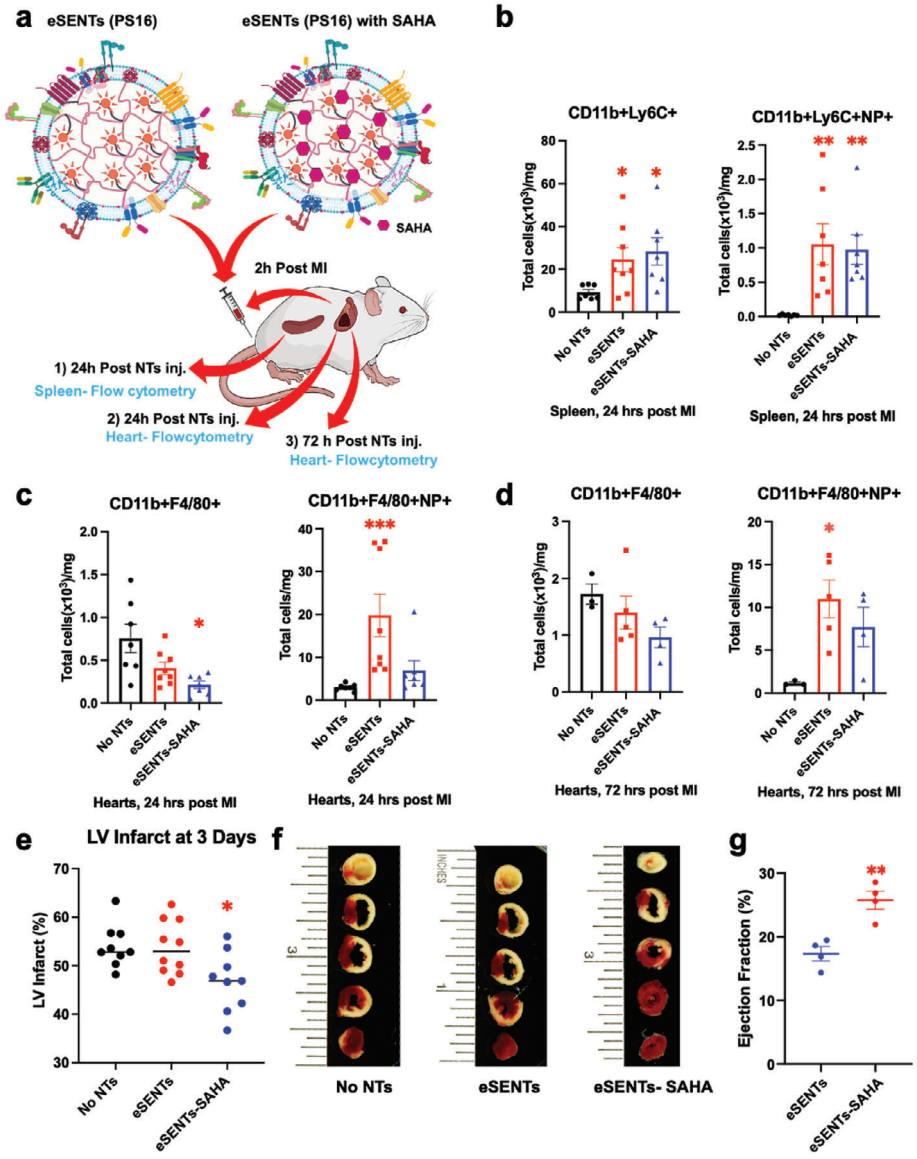

Figure 5. Investigation of the splenic immunocyte-mediated immunomodulatory potential of SAHA-eSENTs. a) Schematic representation of the overall experimental approach. b) Flow cytometry-based quantitation of CD11b+Ly6C+ and CD11b Ly6C+NTs+ (cells that have engulfed CyAl5-eSENTS) within the spleens of CD1 mice receiving MI (cells mg^{-1} spleen tissue, no NTs (saline, $n = 7$), eSENTs alone ($n = 7$), eSENTs-SAHA ($n = 8$)). Flow cytometry-based quantification of CD11b+F4/80+ and CD11b+F4/80+NTs+ (cells that have engulfed CyAl5-eSENTs) in infarcted murine hearts (cells mg^{-1} infarct tissue). c) 24 h post (No NTs ($n = 7$), eSENTs ($n = 8$), eSENTs-SAHA ($n = 7$)), and d) 72 h post-MI (No NTs ($n = 3$), eSENTs ($n = 4$), and eSENTs-SAHA ($n = 5$). e) Quantitative assessment infarct area at 72 h post-MI by TTC staining depicting a 14% decrease in infarct size in the treated group (No NTs ($n = 10$), eSENTs ($n = 10$), eSENTs-SAHA ($n = 9$), $P = 0.04$). f) Representative images of yellow/white region indicate an area of infarction at 72 h post-MI. Infarct areas were measured using ImageJ software. g) Mice were treated daily with either eSENTs-SAHA ($n = 4$) or empty eSENTs ($n = 4$). Mice were subjected to echocardiogram to assess cardiac function as measured by ejection fraction before MI and 7-days post MI. All data are represented as mean±SEM. *p value <0.05, **p value <0.005, and ***p value <0.0005 versus control as determined by Kruskal–Wallis nonparametric analysis with Dunn's multiple comparison post-hoc test or Student's t-test.

3. Conclusions

Biomimicry, especially cell mimicry, is extensively utilized in hybrid nanomaterial development as it possesses the ability to emulate the natural homing capabilities of their source materials.[26,60,65] Here, we have for the first time, demonstrated senescent erythrocyte nano-biomimicry and their potential immunomodulation in cardiovascular disease settings. As shown in the present study, the engineering of senescent erythrocyte membranes facilitates the retention of eSENTs within the spleen, likely through the presentation of "find me" and "eat me" signals on the nanoagent surface while concomitantly decreasing the presence of "don't eat me" signals, such as CD47. When loaded with HDAC inhibitors, splenic retention of the nanomaterials promotes immunomodulation via the cardiosplenic axis, specifically, eSENTs produce an immunomodulatory response by

augmentation of splenic monocyte response in the setting of myocardial injury, reducing infarct size by 14% at a dose 33-fold lower than required to elicit a comparable effect when given systemically. While this reduction may seem modest, it is in relation to the total infarct area. Myocardial infarction causes massive cell death in ischemic areas, and initiates inflammatory and repair processes which result in the formation of a scar as a means to prevent rupture. Areas adjacent to the infarct in the border zone between the necrotic tissue and healthy tissues are thought to be "at risk," with the intensity of the inflammatory process determining the ultimate infarct size. It is this tissue that we are salvaging, thus our observed therapeutic effect is indeed significant.

While the experiments demonstrated herein serve as an initial validation of this platform, and are consistent with our hypothesis, further investigation is currently underway to define the mechanisms relevant to the observed therapeutic benefits. The inflammatory response after MI is multifaceted, and while our initial study has focused on monocyte trafficking, other cell types, including neutrophils, T, B, and dendritic cells are bound to play a role in this process, particularly those cells contained within the splenic milieu. Apart from the cell-specific effects, we are also highly interested in exploring how the localization of SAHA to the spleen modulates monocyte trafficking to the infarct, and are aiming to examine alterations in cytokine profiles and the cell types within the spleen, heart and blood, as well as other reservoirs for these cells including lymph nodes and the bone marrow. While this initial study showed a significant decrease in infarct size and preservation of cardiac function, we would also like to explore how the therapeutic efficacy of our agents might be increased. Likely points of investigation may also include the timing of administration, the dose given, or potentially giving multiple doses. We have also begun considering possible safety concerns that may arise in using these materials. Since they are derivative of RBCs, there is the potential for deleterious activation of the coagulation or complement cascades.[66–67] As with any nanocarrier, unintended biocompatibility issues may arise enroute to potential clinical use, each of which will be considered as we further examine these materials.[68] As opposed to other cell-based source materials, erythropoiesis generates red blood cells by the billions each day. When used in combination with our cFT process, patient-specific nanomaterials can be generated which may facilitate innovative treatment regimens while avoiding potential immunogenicity. In looking beyond MI, several other (auto)immune disorders have splenic manifestations, including systemic lupus erythematosus, for which there are no curative measures. We believe that spleen-localized immunomodulation may thus play an important role in the provision of novel therapeutic avenues for a wide range of diseases.

4. Experimental Section

In Vivo Animal Study: All animal experiments were approved by the Institutional Animal Care and Use Committee (IACUC) at the Masonic Medical Research Institute (Protocol 2021-04-02-CK02) or the Ralph H. Johnson Department of Veterans Affairs Medical Center (Protocol ACORP 706).

Experimental details, including the materials and methods used, can be found in the Supporting Information.

Supporting Information

Supporting Information is available from the Wiley Online Library or from the author.

Acknowledgements

This work was supported, in part, by the National Institutes of Health under Award Nos. R01HL122238 (J.R.M.), R01HL102368 (M.I.K.), and R21AR081535 (J.R.M. and M.I.K.), by the Department of Veterans Affairs, Veterans Health Administration, Office of Research and Development Award No. BX002327 (D.R.M.), the American Heart Association Transformation Grant Award No. 20TPA35490426 (M.I.K.), the Department of Defense Lupus Impact Award W81XWH-21-1-0784 (M.I.K.), the Lupus and Allied Diseases Association, Inc. (J.R.M. and M.I.K.), the Masonic Medical Research Institute's Halfond-Weil Postdoctoral Fellowship (R.J.C.B.), and the Masonic Medical Research Institute (J.R.M. and M.I.K.).

Conflict of Interest

The authors declare no conflict of interest.

Author Contributions

R.J.C.B., C.W.K., D.R.M., and J.R.M. conceived and designed the experiments; R.J.C.B., C.W.K., T.S., K.H., R.C., S.H., N.O., B.X., V., and T.D. performed the experiments. The manuscript was written by R.J.C.B., C.W.K., T.D., T.S., and N.O., and corrected by the senior authors B.O., M.R., M.I.K., D.R.M., and J.R.M. All authors discussed the results and reviewed the manuscript.

Data Availability Statement

The data that support the findings of this study are available from the corresponding author upon reasonable request.

Keywords

biomimetic nanotechnology, cardiosplenic axis, immunomodulation, lipid engineering, myocardial infarction, splenocytes

Received: May 16, 2023
Revised: October 16, 2023
Published online:

[1] R. E. Mebius, G. Kraal, *Nat. Rev. Immunol.* **2005**, *5*, 606.
[2] S. M. Lewis, A. Williams, S. C. Eisenbarth, *Sci. Immunol.* **2019**, *4*, eaau6085.
[3] V. Bronte, M. J. Pittet, *Immunity* **2013**, *39*, 806.
[4] F. Leuschner, P. Dutta, R. Gorbatov, T. I. Novobrantseva, J. S. Donahoe, G. Courties, K. M. Lee, J. I. Kim, J. F. Markmann, B. Marinelli, P. Panizzi, W. W. Lee, Y. Iwamoto, S. Milstein, H. Epstein-Barash, W. Cantley, J. Wong, V. Cortez-Retamozo, A. Newton, K. Love, P. Libby, M. J. Pittet, F. K. Swirski, V. Koteliansky, R. Langer, R. Weissleder, D. G. Anderson, M. Nahrendorf, *Nat. Biotechnol.* **2011**, *29*, 1005.
[5] F. K. Swirski, M. Nahrendorf, M. Etzrodt, M. Wildgruber, V. Cortez-Retamozo, P. Panizzi, J.-L. Figueiredo, R. H. Kohler, A. Chudnovskiy, P. Waterman, E. Aikawa, T. R. Mempel, P. Libby, R. Weissleder, M. J. Pittet, *Science* **2009**, *325*, 612.

[6] G. V. Halade, P. C. Norris, V. Kain, C. N. Serhan, K. A. Ingle, *Sci. Signal.* **2018**, *11*, eaao1818.
[7] S. B. Gowda, D. Gowda, V. Kain, H. Chiba, S.-P. Hui, C. E. Chalfant, V. Parcha, P. Arora, G. V. Halade, *Am. J. Physiol.: Heart Circ. Physiol.* **2021**, *321*, H599.
[8] F. Wang, R. Zong, G. Chen, *J. Controlled Release* **2022**, *341*, 314.
[9] G. Heusch, *Circ. Res.* **2019**, *124*, 26.
[10] F. Leuschner, P. Panizzi, I. Chico-Calero, W. W. Lee, T. Ueno, V. Cortez-Retamozo, P. Waterman, R. Gorbatov, B. Marinelli, Y. Iwamoto, A. Chudnovskiy, J.-L. Figueiredo, D. E. Sosnovik, M. J. Pittet, F. K. Swirski, R. Weissleder, M. Nahrendorf, *Circ. Res.* **2010**, *107*, 1364.
[11] P. Li, J. Ge, H. Li, *Nat. Rev. Cardiol.* **2020**, *17*, 96.
[12] D. Kimbrough, S. H. Wang, L. H. Wright, S. K. Mani, H. Kasiganesan, A. C. Larue, Q. Cheng, S. N. Nadig, C. Atkinson, D. R. Menick, *J. Mol. Cell. Cardiol.* **2018**, *119*, 51.
[13] T. G. Gillette, J. A. Hill, *Circ. Res.* **2015**, *116*, 1245.
[14] T. G. Gillette, *Am. Heart Assoc.* **2021**, *143*, 1891.
[15] M. Wallner, D. Eaton, R. Berretta, J. Wu, M. Jeong, Y. Lin, G. Borghetti, S. Baker, H. Zhao, M. Oyama, *Circulation* **2018**, *138*, A13151.
[16] M. Y. Jeong, Y. H. Lin, S. A. Wennersten, K. M. Demos-Davies, M. A. Cavasin, J. H. Mahaffey, V. Monzani, C. Saripalli, P. Mascagni, T. B. Reece, A. V. Ambardekar, H. L. Granzier, C. A. Dinarello, T. A. Mckinsey, *Sci. Transl. Med.* **2018**, *10*, eaao0144.
[17] J. G. Travers, S. A. Wennersten, B. Peña, R. A. Bagchi, H. E. Smith, R. A. Hirsch, L. A. Vanderlinden, Y.-H. Lin, E. Dobrinskikh, K. M. Demos-Davies, *Circulation* **2021**, *143*, 1874.
[18] S. K. Mani, C. B. Kern, D. Kimbrough, B. Addy, H. Kasiganesan, W. T. Rivers, R. K. Patel, J. C. Chou, F. G. Spinale, R. Mukherjee, D. R. Menick, *Am. J. Physiol.: Heart Circ. Physiol.* **2015**, *308*, H1391.
[19] V. R. Muzykantov, *Expert Opin. Drug Delivery* **2013**, *10*, 23176316.
[20] C. H. Villa, D. C. Pan, I. H. Johnston, C. F. Greineder, L. R. Walsh, E. D. Hood, D. B. Cines, M. Poncz, D. L. Siegel, V. R. Muzykantov, *Blood Adv.* **2018**, *2*, 165.
[21] C. H. Villa, A. C. Anselmo, S. Mitragotri, V. Muzykantov, *Adv. Drug Delivery Rev.* **2016**, *106*, 88.
[22] D. C. Pan, J. W. Myerson, J. S. Brenner, P. N. Patel, A. C. Anselmo, S. Mitragotri, V. Muzykantov, *Sci. Rep.* **2018**, *8*, 1615.
[23] P. M. Glassman, C. H. Villa, A. Ukidve, Z. Zhao, P. Smith, S. Mitragotri, A. J. Russell, J. S. Brenner, V. R. Muzykantov, *Pharmaceutics* **2020**, *12*, 440.
[24] K. E. Badior, J. R. Casey, *IUBMB Life* **2018**, *70*, 32.
[25] M. Freesmeyer, S. Gröber, J. Greiser, P. Seifert, F. Gühne, R. Drescher, *Eur. J. Nucl. Med. Mol. Imaging* **2021**, *48*, 644.
[26] R. J. C. Bose, S.-H. Lee, H. Park, *Drug Discovery Today* **2016**, *21*, 1303.
[27] Y. Matsusaka, T. Nakahara, K. Takahashi, Y. Iwabuchi, Y. Ogata, C. Nishime, M. Kajimura, M. Jinzaki, *Nucl. Med. Biol.* **2018**, *56*, 26.
[28] R. R. Armas, M. L. Thakur, A. Gottschalk, *J. Nucl. Med.* **1980**, *21*, 413.
[29] I. Safeukui, P. A. Buffet, G. Deplaine, S. Perrot, V. Brousse, A. Sauvanet, B. Aussilhou, S. Dokmak, A. Couvelard, D. Cazals-Hatem, O. Mercereau-Puijalon, G. Milon, P. H. David, N. Mohandas, *Blood Adv.* **2018**, *2*, 2581.
[30] V. Pallotta, G. M. D'amici, A. D'alessandro, R. Rossetti, L. Zolla, *Blood Cells, Mol., Dis.* **2012**, *48*, 226.
[31] C. Stoll, W. F. Wolkers, *Transfus. Med. Hemother.* **2011**, *38*, 89.
[32] W. F. Wolkers, S. K. Balasubramanian, E. L. Ongstad, H. C. Zec, J. C. Bischof, *Biochim. Biophys. Acta Biomembr.* **2007**, *1768*, 728.
[33] P. L. Rodriguez, T. Harada, D. A. Christian, D. A. Pantano, R. K. Tsai, D. E. Discher, *Science* **2013**, *339*, 971.
[34] P.-A. Oldenborg, A. Zheleznyak, Y.-F. Fang, C. F. Lagenaur, H. D. Gresham, F. P. Lindberg, *Science* **2000**, *288*, 2051.
[35] P. Arese, F. Turrini, E. Schwarzer, *Cell. Physiol. Biochem.* **2005**, *16*, 133.
[36] N. Arashiki, N. Kimata, S. Manno, N. Mohandas, Y. Takakuwa, *Biochemistry* **2013**, *52*, 5760.
[37] H. U. Lutz, F. Bussolino, R. Flepp, S. Fasler, P. Stammler, M. D. Kazatchkine, P. Arese, *Proc. Natl. Acad. Sci. USA* **1987**, *84*, 7368.
[38] A. B. Zaltzman, C. W. Van Den Berg, V. R. Muzykantov, B. P. Morgan, *Biochem. J.* **1995**, *307*, 651.
[39] V. R. Muzykantov, M. D. Smirnov, A. L. Klibanov, *J. Immunol. Methods* **1993**, *158*, 183.
[40] V. R. Muzykantov, M. D. Smirnov, A. L. Klibanov, *FEBS Lett.* **1993**, *318*, 108.
[41] V. R. Muzykantov, J. C. Murciano, R. P. Taylor, E. N. Atochina, A. Herraez, *Anal. Biochem.* **1996**, *241*, 109.
[42] J. H. Lorent, K. R. Levental, L. Ganesan, G. Rivera-Longsworth, E. Sezgin, M. Doktorova, E. Lyman, I. Levental, *Nat. Chem. Biol.* **2020**, *16*, 644.
[43] J. T. Dodge, G. B. Phillips, *J. Lipid Res.* **1967**, *8*, 667.
[44] A. J. Schroit, J. W. Madsen, Y. Tanaka, *J. Biol. Chem.* **1985**, *260*, 5131.
[45] P. Munder, M. Modolell, R. Andreesen, H. Weltzien, O. Westphal, *Springer Semin. Immunopathol.* **1979**, *2*, 187.
[46] S. T. Tan, T. Ramesh, X. R. Toh, L. N. Nguyen, *Prog. Lipid Res.* **2020**, *80*, 101068.
[47] L.-R. Montes, D. J. López, J. Sot, L. A. Bagatolli, M. J. Stonehouse, M. L. Vasil, B. X. Wu, Y. A. Hannun, F. M. Goñi, A. Alonso, *Biochemistry* **2008**, *47*, 11222.
[48] H. Ahyayauch, A. B. García-Arribas, J. Sot, E. J. González-Ramírez, J. V. Busto, B. G. Monasterio, N. Jiménez-Rojo, F. X. Contreras, A. Rendón-Ramírez, C. Martin, A. Alonso, F. M. Goñi, *Sci. Rep.* **2018**, *8*, 7456.
[49] F. E. Boas, L. Forman, E. Beutler, *Proc. Natl. Acad. Sci. USA* **1998**, *95*, 3077.
[50] R. Schlegel, P. Williamson, *Cell Death Differ.* **2001**, *8*, 551.
[51] Y. T. Sato, K. Umezaki, S. Sawada, S. Mukai, Y. Sasaki, N. Harada, H. Shiku, K. Akiyoshi, *Sci. Rep.* **2016**, *6*, 21933.
[52] R. J. C. Bose, N. Tharmalingam, F. J. Garcia Marques, U. K. Sukumar, A. Natarajan, Y. Zeng, E. Robinson, A. Bermudez, E. Chang, F. Habte, S. J. Pitteri, J. R. Mccarthy, S. S. Gambhir, T. F. Massoud, E. Mylonakis, R. Paulmurugan, *ACS Nano* **2020**, *14*, 5818.
[53] S. Himbert, M. J. Blacker, A. Kihm, Q. Pauli, A. Khondker, K. Yang, S. Sinjari, M. Johnson, J. Juhasz, C. Wagner, H. D. H. Stöver, M. C. Rheinstädter, *Adv. Biosyst.* **2020**, *4*, 1900185.
[54] S. Himbert, S. M. Qadri, W. P. Sheffield, P. Schubert, A. D'alessandro, M. C. Rheinstädter, *PLoS One* **2021**, *16*, 0259267.
[55] S. Himbert, I. P. Gastaldo, R. Ahmed, K. M. Pomier, B. Cowbrough, D. Jahagirdar, S. Ros, J. Juhasz, H. D. H. Stöver, J. Ortega, G. Melacini, D. M. E. Bowdish, M. C. Rheinstädter, *PLoS One* **2022**, *17*, 0263671.
[56] H. Krivic, S. Himbert, R. Sun, M. Feigis, M. C. Rheinstädter, *ACS Infect. Dis.* **2022**, *8*, 2059.
[57] H. I. Ingólfsson, M. N. Melo, F. J. Van Eerden, C. Arnarez, C. A. Lopez, T. A. Wassenaar, X. Periole, A. H. De Vries, D. P. Tieleman, S. J. Marrink, *J. Am. Chem. Soc.* **2014**, *136*, 14554.
[58] S. Himbert, R. J. Alsop, M. Rose, L. Hertz, A. Dhaliwal, J. M. Moran-Mirabal, C. P. Verschoor, D. M. E. Bowdish, L. Kaestner, C. Wagner, M. C. Rheinstädter, *Sci. Rep.* **2017**, *7*, 39661.
[59] Y. Kim, M. E. Lobatto, T. Kawahara, B. Lee Chung, A. J. Mieszawska, B. L. Sanchez-Gaytan, F. Fay, M. L. Senders, C. Calcagno, J. Becraft, M. Tun Saung, R. E. Gordon, E. S. G. Stroes, M. Ma, O. C. Farokhzad, Z. A. Fayad, W. J. M. Mulder, R. Langer, *Proc. Natl. Acad. Sci. USA* **2014**, *111*, 1078.
[60] R. J. Bose, B. J. Kim, Y. Arai, I.-B. Han, J. J. Moon, R. Paulmurugan, H. Park, S.-H. Lee, *Biomaterials* **2018**, *185*, 360.
[61] B. Ouyang, W. Poon, Y.-N. Zhang, Z. P. Lin, B. R. Kingston, A. J. Tavares, Y. Zhang, J. Chen, M. S. Valic, A. M. Syed, P. Macmillan, J. Couture-Senécal, G. Zheng, W. C. W. Chan, *Nat. Mater.* **2020**, *19*, 1362.
[62] L. Yang, Y. Ye, L. Cai, *Signal. Transduc. Targeted Ther.* **2020**, *5*, 272.

[63] I. Hilgendorf, L. M. S. Gerhardt, T. C. Tan, C. Winter, T. A. W. Holderried, B. G. Chousterman, Y. Iwamoto, R. Liao, A. Zirlik, M. Scherer-Crosbie, C. C. Hedrick, P. Libby, M. Nahrendorf, R. Weissleder, F. K. Swirski, *Circ. Res.* **2014**, *114*, 1611.
[64] M. Nahrendorf, M. J. Pittet, F. K. Swirski, *Circulation* **2010**, *121*, 2437.
[65] C.-M. J. Hu, L. Zhang, S. Aryal, C. Cheung, R. H. Fang, L. Zhang, *Proc. Natl. Acad. Sci. USA* **2011**, *108*, 10980.
[66] C. H. Villa, J. Seghatchian, V. Muzykantov, *Transfus. Apher. Sci.* **2016**, *55*, 275.
[67] D. Pan, O. Vargas-Morales, B. Zern, A. C. Anselmo, V. Gupta, M. Zakrewsky, S. Mitragotri, V. Muzykantov, *PLoS One* **2016**, *11*, 0152074.
[68] M. Howard, B. J. Zern, A. C. Anselmo, V. V. Shuvaev, S. Mitragotri, V. Muzykantov, *ACS Nano* **2014**, *8*, 4100.